Journal of
Materials Chemistry A

Accepted Manuscript

Optical Quantum Confinement in Low Dimensional Hematite

Mattis Fondell, T. Jesper Jacobsson, Mats Boman and Tomas Edvinsson*
Department of Chemistry - Ångström Laboratory, Uppsala University, Box 538, 75121 Uppsala, Sweden

Dept. of Chemistry - Ångström Laboratory, Uppsala University, Box 538, 75121 Uppsala, Sweden
Tomas.edvinsson@kemi.uu.se

Abstract

Hematite is considered as a promising material for various applications, including for example photo-electrochemical cells for solar hydrogen production. Due to limitations in the charge transport properties hematite needs to be in the form of low-dimensional particles or thin films in several of these applications. This may however affect the optical properties, introducing additional complications for efficient design of photo active devices. In this paper the optical absorption is analyzed in detail as a function of film thickness for 35 thin films of hematite ranging between 2 and 70 nm. The hematite was deposited by atomic layer deposition on FTO-substrates using $Fe(CO)_5$ and O_2 as precursors. It was found that for film thicknesses below 20 nm the optical properties are severely affected as a consequence of quantum confinement. One of the more marked effects is a blue shift of up to 0.3 eV for thinner films of both the indirect and direct transitions, as well as a 0.2 eV shift of the absorption maximum. The data show a difference in quantum confinement for the indirect and the direct transitions, where the probability for the indirect transition decreases markedly and essentially disappears for the thinnest films. Raman measurements showed no peak shift or change in relative intensity for vibrations for the thinnest films indicating that the decrease in indirect transition probability not could be assigned to depression of any specific phonon but instead seems to be a consequence of isotropic phonon confinement. The onset of the indirect transition is found at 1.75 eV for the thickest films and shifted to 2.0 eV for the thinner films. Two direct transitions are found at 2.15 eV and 2.45 eV, which are blue shifted 0.3 and 0.45 eV respectively, when decreasing the film thickness from 20 to 4 nm. Low dimensional hematite, with dimensions small enough for efficient charge transport, thus has a substantially lower absorption in the visible than expected from bulk values. This knowledge of the intrinsic optical behavior for low dimensional hematite will be of importance in the design of efficient photo active devices.

Keywords

Iron oxide, Hematite, Fe_2O_3, indirect transition, quantum confinement, low dimensional. ultrathin films, ALD

1. Introduction

By being the most common form of iron oxide and one of the main components of iron ore hematite is of immense importance to our industrialized society. In the presence of rust it is also one of few semiconductors visible, although not appreciated, in everyday life. Despite this it turns out that behind the familiar rusty façade our understanding of the material properties is insufficient with respect to the technological expectation set upon the material. One such example concerns the fundamental optical properties, like how the quantum confinement effects the direct and indirect optical transitions in low dimensional nanostructures, which currently are investigated for a number of promising high tech applications.

Nanoscale hematite is suggested to find use in for example lithium ion batteries[1, 2], cleaning of water[3], cancer treatment[4] and gas sensors[5] to mention a few possible applications. Hematite also demonstrates a set of close to ideal properties for photoassisted water splitting which have motivated a lot of research[6-10]. The band gap of approximately 2 eV is reasonable high in order to obtain the necessary overpotential while still allowing for absorption in the visible range. The absorption coefficient is reasonably high and the energetic position of the valence band edge is suitable for water oxidation. It is, as evident by the widespread appearance of rust, highly stable in ambient environment and composed of abundant, cheap and nontoxic elements.

The conduction band energy is somewhat too low for unassisted hydrogen production and hematite is mainly investigated as a photoanode. The Achilles heel for hematite turns out to be the charge carrier transport, especially of the minority carriers. The diffusion length of photogenerated holes is in the nanometer range[6], which is substantially less than the few hundred nanometers needed for absorption of the majority of the green and red light in the solar spectrum. To reach high internal quantum efficiency the thickness of hematite layers thus needs to be substantially thinner than what is needed to absorb a sufficient amount of the incoming light. A strategy explored in the literature for overcoming this obstacle is to ortogonalize the process of absorption and charge transport by various types of nanostructuration[11]. For this purpose much work is devoted towards synthesis of different hematite nanostructures like nanorods[12], nanotubes[13], dendritic systems[14] and mesoporous systems[15] to mention a few.

In order to optimize efficient nanostructures for water oxidation, more fundamental knowledge is needed concerning the photo physics of low dimensional hematite. It is reasonable to assume that both the optical and the transport properties deviate from the bulk values for nanostructures as a consequence of quantum confinement. A blue shift in the absorption edge for smaller structures has for example been reported both for nanorods[16] and mesoporous structures[15]. Hematite is also known to change color depending on size, shape and synthesis condition[17], which have been attributed to both quantum size effects and shape dependent reflectance[9]. For very small particles and ultrathin films, also the choice of substrate is important and effects the possible iron oxide phases that can be formed[18]. A better understanding of these dependencies would be of importance for the design of new and more complex nanostructures, and would give insight into what could be expected in terms of ideal efficiency for a given structure.

The motivation behind this work is to increase the understanding for thickness dependent absorption properties for both the indirect and direct transitions in hematite, which are important in for example solar assisted water oxidation as well as other photocatalytic processes. Ultrathin films are rather non-complex systems compared to rods or dendritic structures, making it easier to perform measurements from which more general conclusions can be drawn. Conclusions which in many cases can be transferable to more complex

nanostructures, where properties deriving from low dimensionality otherwise can be hard to separate from properties induced by the increased surface area and shape dependent reflectance.

Several possible synthesis routes towards hematite are described in the literature ranging from oxidation of iron[19], hydrothermal synthesis[20], sol gel[21], electrochemical deposition[22], ultrasonic spray pyrolysis[23] and various gas phase routs like atomic layer deposition, ALD[24], and chemical vapor deposition, CVD[25]. In this work hematite films have been deposited by an ALD sequence, which have the advantage of enable synthesis on flat substrates as well as on highly complicated three dimensional structures. The results obtained here for flat films, naturally selecting a higher limit of the possible sizes of the grains, should thus with the same synthesis technique be applicable to nanostructured substrates. The paper starts with a short theory section which illuminates the different approximations made in the conventional equations for extracting the direct and indirect band gap. This is followed by details on the synthesis, materials characterization and an in-depth analysis of the thickness dependence of the optical properties including the relation between the direct and indirect transitions.

2. Theory

In order to analyze the optical transitions in hematite in some detail it is appropriate to illuminate the different approximations involved while deriving the conventional energy scaling dependences for the direct and indirect transitions. This is valuable since it adds a critical view of what is obtained while analyzing absorption data in order to extract direct and indirect band gaps.

In a simple quantum mechanical model the absorption and creation of photogenerated charge carriers can be viewed as a time-dependent polarization of the electron. The time-dependent Schrödinger equation for the interaction between the incoming electromagnetic field, *A*, and an electron is then given by eqn. (1)[26]

$$\left[H_0(\boldsymbol{r})+H'(t)\right]\psi=\left[\frac{\boldsymbol{p}^2}{2m_0}+\boldsymbol{V}(r)-\frac{e}{m_0}\boldsymbol{p}\cdot\boldsymbol{A}\right]\psi=i\hbar\frac{\partial\psi}{\partial t} \quad (1)$$

where H_0 is the unperturbed Hamiltonian, $\hbar$ is the reduced Planck's constant, m_0 the electron mass, e the electron charge, p the electron momentum, V the potential, t time and ψ the electron wave function. The factor $-e\cdot\boldsymbol{p}\cdot\boldsymbol{A}/m_0$ correspond to the time-dependent perturbation, $H'(t,)$ from the incoming oscillating electromagnetic field. The general solution to the time dependent Schrödinger equation $H_0\psi = i\hbar\partial\psi/\partial t$ is given by eqn. (2)

$$\psi(\boldsymbol{r},t)=\sum_j c_j(t)\psi(\boldsymbol{r})\exp\left(-iE_jt/\hbar\right) \quad (2)$$

where E_j is the energy of the j:th state with the weighting factor c_j. The coefficients c_j are given by solving the perturbation equation given in eqn. (1). In a two state model with the initial state, *i*, and the final state, *f*, the transition probability from the initial to the final state, $T_{i\rightarrow f}$, is given by the time derivative of the square of the weighting coefficient c_f [27]. Using the solution for c_f and assuming a long interaction time then gives eqn. (3) for the transition probability

$$T_{i\rightarrow f}=\frac{d}{dt}\left|c_f(t)\right|^2=\frac{2\pi t}{\hbar^2}\left|H'_{if}\right|^2\delta\left(E_f-E_i-\hbar\omega\right) \quad (3)$$

where H'_{if} is the overlap matrix between the initial and final state, E_i and E_f the energy of the initial and final state respectively and $\hbar\omega$ the energy of the incoming photon representing the perturbation. Here the delta function, δ, gives the energy for where absorption occurs whereas the prefactor containing the overlap matrix gives the amplitude of the transition. This transition rate per unit time is referred to as the Fermi golden rule with the origin in perturbation theory within the two state approximation by Dirac[28]. For a crystal the situation gets more complex. The initial and final state will be represented by the valence and conduction band, E_v and E_c, respectively and both will constitute a distribution of states in *k*-space rather than being single states. The Fermi golden rule and the equivalent of the two state approximation for a crystal [29] then gives eqn. (4)

$$T_{v\rightarrow c}=\frac{d}{dt}\left|c_c(t)\right|^2=\frac{2\pi}{\hbar}\int_{BZ}\frac{1}{4\pi^3}\left|H'_{vc}\right|^2\delta\left(E_c(\boldsymbol{k})-E_v(\boldsymbol{k})-\hbar\omega\right)dk \quad (4)$$

where the integration is performed over the first Brillouin zone, *BZ*, and where the normalization factor $1/4\pi^3$ comes from the $2/\Omega$ number of spin states per unit volume, $8\pi^3/\Omega$, of the primitive lattice cell. In the case of direct transition there is no change in the crystal momentum ($k=0$) between the initial and final states as illustrated in figure 1.a and 1.b. The perturbation matrix element can then be considered independent of the *k*-vector within the first *BZ* when the wavelength of the perturbing light is much larger than the dimensions of the interaction volume in the *BZ*. H'_{vc} can then be placed outside the integration transforming eqn. (4) to eqn. (5)

$$T_{v\to c} = \frac{2\pi}{\hbar}\left|H'_{vc}\right|^2 \int_{BZ} \frac{1}{4\pi^3}\delta\left(E_c - E_v - \hbar\omega\right)d\boldsymbol{k} \tag{5}$$

where the integral can be written as eqn. (6)

$$\int_{BZ} \frac{1}{4\pi^3}\delta\left(E_c - E_v - \hbar\omega\right)d\boldsymbol{k} = g_{vc}\left(\hbar\omega\right) \tag{6}$$

where $g_{vc}(\hbar\omega)$ is the joint density of states, which basically is the combination of donor states in the valence band and acceptor states in the conduction band. In a first approximation the electrons and holes can for energies close to the band edges be described as particles obeying the energy of an harmonic potential, but with a modified or effective mass correcting for resistance to movement in the lattice. The valence and conduction band energies then get a parabolic dependence on the crystal momentum, *k*, according to eqn. (7) and eqn. (8)

$$E_v(k) = E_v(0) - \frac{\hbar^2 k^2}{2m_p^*} \tag{7}$$

$$E_c(k) = E_c(0) + \frac{\hbar^2 k^2}{2m_n^*} \tag{8}$$

where $E_v(0)$ and $E_c(0)$ are the energy for the valence and conduction band edge at the Γ-point and where m_n^* and m_p^* are the effective masses of the electrons and the holes. This is often a fully adequate description in a limited energy range close to the band edges. In this parabolic approximation the joint density of states can be worked out (see supporting information) which together with eqn. (5) give eqn. (9) for the transition probability for a direct transition

$$T_{v\to c} = \frac{2\pi}{\hbar}\left|H'_{vc}\right|^2 g_{cv}\left(\hbar\omega\right) = \left|H'_{vc}\right|^2 \frac{1}{\hbar\pi}\left(\frac{2m_{red}^*}{\hbar^2}\right)^{3/2}\left(\hbar\omega - E_g\right)^{1/2} \tag{9}$$

where $m^*_{red} = m_n^* \cdot m_p^*/(m_n^* + m_p^*)$ is the reduced effective mass and E_g is the band gap energy. The transition probability is essentially the absorption coefficient, and thus directly scaling with the measured absorption. The interaction Hamiltonian has already been assumed to be much larger than the perturbation volume in *k*-space and can thus be considered independent on the incoming energy in a region close to the band gap. The absorption for a direct transition thus scales as the square root of the energy difference between the band gap and the incoming light. This allows the direct band gap to be extracted by plotting the square of the measured absorption and extrapolating down to zero absorption as illustrated in figure 1.c.

Direct transitions are however not the only alternatives seen in crystals, where also indirect transitions occur. These involves a change in momentum, but as the incoming light have a low momentum the photon needs to couple with a phonon for this transition to occur as illustrated in figure 1.b. This essentially represents a two particle interaction and is thus a less likely event compared to the direct transition. It is also more complicated to describe as the interaction Hamiltonian H'_{vc} in eqn. (4) no longer is independent on k and thus not can be taken outside the integral. The initial and final states can in this case be described by eqn. (10) and eqn. (11)

$$E_v = E_{\alpha k} + \hbar\omega_{light} + \hbar\omega_q \tag{10}$$

$$E_c = E_{\beta k+q} \tag{11}$$

where α and β refer to different Bloch bands, $\hbar\omega_{light}$ is the energy of an absorbed photon and $\hbar\omega_q$ is the energy of an absorbed phonon. Including both phonon absorption ($E_{\alpha \mathbf{k}} + \hbar\omega_{\mathbf{q}}$) and emission ($E_{\alpha \mathbf{k}} - \hbar\omega_{\mathbf{q}}$), and integrating over the states one obtains an extra contribution of $(\hbar\omega - E_g)^{3/2}$ for an allowed indirect transition[30] giving the transition probability to scaling with[30, 31] $(\hbar\omega - E_g)^2$. A plot of the energy of the incoming photons, $\hbar\omega_{light}$, versus the square root of the absorption coefficient would thus give the band gap of the indirect transition if extrapolated down to zero absorption as illustrated in figure 1.c. The precise dependence on the type of phonon and how to perform the integration when there is a limited lifetime of the phonons is more complicated[32] and outside the scope of this study.

Within the assumptions made in the outlined derivations a general schematic expression for the transition probability is given in eqn. (12)

$$T_{v\to c} = C_1\left(\hbar\omega - E_g\right)^{\eta} \tag{12}$$

where η = 1/2 for an allowed direct transition and 2 for an allowed indirect transition. This also holds for forbidden direct and indirect transitions where η = 2/3 and 3 respectively[30, 33, 34].

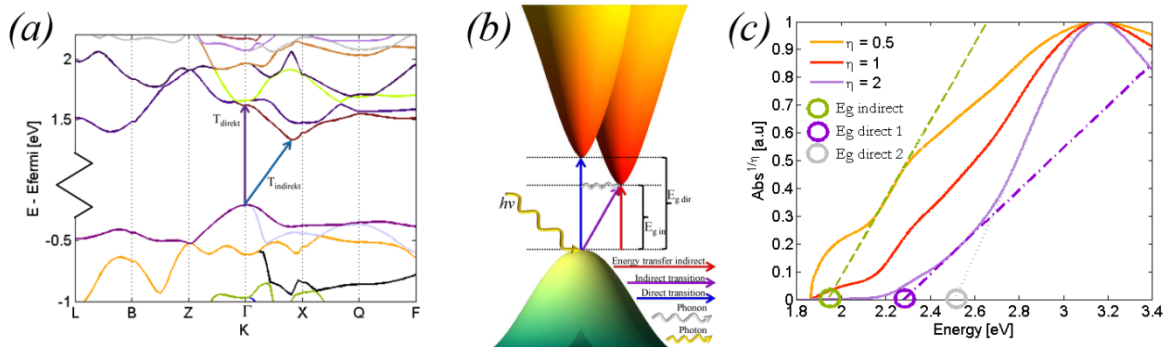

Figure (1). (a) Calculated band diagram for hematite illustrating the direct and the indirect transition. Data is from DFT calculations from Materials Project[35] using GGA+U. (b) Illustration of the parabolic nature of the bands close to the band edges and the phonon transfer involved in an indirect transition. (c) Extraction of optical band gaps according to eqn. (12). Data are normalized in order ease the interpretation.

In the case of thin films and other low dimensional nanostructures the situation is further complicated. An important parameter for thin films, small particles and other nano-geometries is the exciton Bohr radius. This indicates the distance over which an electron in the

conduction band by coulomb forces can interact with a hole in the valence band to such an extent that a bound state is formed. Reduction in dimensionality from 3D to 1D in GaAs and GaN can result in dramatic effects in electronic and optical behavior[36, 37]. The effects for hematite thin films as in this study are less dramatic and can be considered a quasi-2D system if the film thickness is smaller than the exciton Bohr radius in the material, which is referred to as the strong confinement region[38]. If the film thickness is comparable to, or slightly higher than the exciton Bohr radius, it can be seen as a 3D system confined more in the direction of the film thickness. This is referred to as the weak confinement region[38]. These situations can be referred to as strong and weak electronic quantum confinements by comparison of the pseudo-extension of the electrons and holes with the dimension of the particle.

When a material is quantum confined, properties like the band gap, band edge positions, energetic positions of defect levels and the joint density of state tend to change[39-41], which all have an effect on the transition probability for the direct transitions. They tend to be blue shifted and also the amplitude can change. The probability of indirect transitions may be subjected to even larger changes as they also are affected by the properties of the phonons which can be quite different for low dimensional structures[42]. Different phonons can be affected differently and they can be suppressed for structures larger than would experience electronically quantum confinement[42]. For an indirect semiconductor, the total optical quantum confinement would thus be the combined effect of the electronic quantum confinement and the vibrational quantum confinement. Here we will try to distinguish these effects and investigate to what effect the phonon confinement in the thin films of hematite contributes to the optical quantum confinement effects with respect to the indirect transitions in thin films of hematite.

3. Experimental

3.1 Synthesis

The method of atomic layer deposition were developed in the 1970's by Suntola et al.[43], and is today a well-known technology. Compared to other thin film deposition techniques ALD possess a good thickness control with high step coverage achieved by separation of the reactive pulses with a purging pulse. Each precursor pulse is self-limiting to the surface making a layer by layer growth possible. The most common ALD cycle consist of four pulses. The first is a precursor pulse followed by a purge pulse, a second precursor pulse and ends with a second purge pulse. When the experimental parameters: temperature, pressure and gas flow are chosen properly the number of cycles determines the thickness of the deposited film.

In this work all films were deposited in a Picosun Sunale (R-series) ALD unit. Iron pentacarbonyl, $Fe(CO)_5$, was used as the iron precursor, and chosen because of a suitable vapor pressure[44], and because it is a liquid at room temperature. This is beneficial compared to iron precursors for ALD previously described in the literature that have been solids with either higher evaporation temperature[45] or poor deposition rate[46]. A summary of different precursors previously used in ALD synthesis of iron oxides are found in table 1. $Fe(CO)_5$ has previously been reported as a precursor for CVD[14, 47] but no ALD references were found. The $Fe(CO)_5$ was purchased from Fisher Scientific with a purity of 99.5%. The liquid was put in a 75 ml container purchased from Swagelok and was cooled to 12°C. The oxygen precursor used was O_2 gas from in house with a purity of ~99.998%.

Table 1: Summary of precursors reported for ALD synthesis of iron oxides

Iron Precursor	Oxygen Precursor	Reference
$FeCl_3$	H_2O	45
$Fe(acac)_3$	O_2	48
$Fe(acac)_3$	O_3	49
$Fe(thd)_3$	O_3	46, 50-52
$Fe(Cp)_2$	O_2	53-55
$Fe(Cp)_2$	O_3	56-58
$Fe(^tBuAMD)_2$	H_2O	59
$Fe_2(^tBuO)_6$	H_2O	56, 60, 61

Carbon monoxide, CO, was used as carrier gas in order to reduce the amount of decomposition of the $Fe(CO)_5$ into CO and $Fe(CO)_x$, and was continuously flowing during the deposition. The CO used was purchased from Air Liquide with a purity of 99.5%. N_2 was used during heating and cooling of the system. The $Fe(CO)_5$ had a tendency to decompose in the inlet to the reactor chamber. This part, consisting of a glass tube with an inner diameter of 4 mm, was changed after each run. The pulse times was 0.1 – 5 – 3 – 5 seconds and were kept constant during the test series. The thickness was controlled by changing the number of cycles between 50 and 600. The deposition temperature where set at 300°C in order to form hematite, α-Fe_2O_3. The pressure in the deposition chamber was 5 Torr.

Depositions were made on both Si(100) and fluorine doped tin oxide, FTO. Silicon has the advantage of being an atomically smooth substrate, whereas FTO enables both transient absorption and electrochemical measurements. During each experiment depositions were made on six Si samples (~2·2cm) and five FTO samples (~2·1cm). The substrates were cleaned in ethanol in an ultrasonic bath for 15 minutes and then dried under N_2-flow. All films were annealed for 8h at 500°C in air. Step of 5°C/min was used when heating whereas cooling was done over night.

3.2 Material characterization

X-ray diffraction, XRD, were measured in both gracing incidence, GIXRD, and theta-2theta mode. The GIXRD was used for the thinnest films on Si(100). The films deposited on FTO were measured with theta-2theta scans as the surface roughness obstructed the GIXRD measurement. The theta-2theta scans were made on a Bruker D8 Advance and the GIXRD was done on a D5000 Siemens instrument. In both cases Cu Kα radiation with λ=1.54Å was used.

The volume averaged film thickness deposited on Si(100) where measured with X-ray reflectivity, XRR, while elemental composition was obtained from X-Ray Fluorescence, XRF, measurements. By knowing the influence of the substrate to the Fe-Kα peak the absolute iron amount were calculated. From these measurements a calibration-curve with XRR-thickness versus XRF-intensity was constructed which is given in the supporting information. The high surface roughness of FTO prevents films thicknesses to be extracted from XRR measurements in the current setup. An initial estimation of the film-thicknesses on the FTO substrates was instead based on XRF measurements using the calibration curve based on XRF and XRR measurements made on films deposited on Si(100).

The XRF measurements were performed on a PANalytical Epsilon 5 instrument with a Germanium target and a spot size of ~1 cm. XRR measurements were done on a D5000 Siemens with Cu Kα radiation and analyzed in the reflectivity software X'pert reflectivity from PANalytical.

Imaging was done by a Zeiss LEO 1550 Scanning electron microscope with an acceleration voltage of 5 keV. The films were also analyzed with X-ray photoelectron spectroscopy, XPS, using a PHI Quantum 2000 ESCA with an analyzing spot of 200·200μm. For sputtering an argon sputter with acceleration voltage of 500V spot size of ~1·1mm and step time of 0.5 min was used. Raman spectroscopy measurements were performed on a Renishaw micro Raman system 2000 using the 514 nm line of an argon-ion laser. UV-vis absorption measurements were performed on an Ocean Optics spectrophotometer HR-2000+ with deuterium and halogen lamps. In all measurements, a full spectrum from 190 to 1100 nm with 2048 evenly distributed points was sampled. In order to obtain good statistics an average of over 10000 consecutive spectra were done. To further reduce the noise in the signal an average moving filter was applied.

4. Results and discussion

4.1 Synthesis

During the synthesis, $Fe(CO)_5$ decomposed in the reaction chamber at 300°C. The decomposition of the iron precursor occurred for temperatures as low as 100°C posing some challenges for the synthesis. In order to decrease the problem of precursor decomposition, CO was used as carrier gas. This decreased the problem even though some decomposition still was visible at the chosen deposition temperature. Another effect of CO was a continuous reduction of the surface, initially producing a phase mixture of magnetite, Fe_3O_4, and maghemite, γ-Fe_2O_3. All the films were therefore post-annealed for 8h at 500°C in air, which gave phase pure hematite films without any detectable presence of magnetite or maghemite.

Due to decomposition of the precursor both before and at the inlet to the reaction chamber, as well as partial nucleation problems at the surface, a constant slope for the thickness/number-of-cycles for the samples could not be extracted. The thickness, however, increased with increased number of cycles, and at a slightly higher rate than expected for a pure ALD synthesis. The synthesis would therefore rather be described as an ALD-hybrid, where the precursors are pulsed like ALD but where the growth rate is somewhat higher than in normal ALD, and thus approaching chemical vapor deposition, CVD.

A total of 35 samples with different film thicknesses were deposited on FTO, from which the absorption properties could be investigated.

4.2 Material characterization

The as deposited films were prior to annealing composed of maghemite and/or magnetite as illustrated by the GIXRD spectrum of films deposited on Si(100) in figure 2.a. After annealing the films in 500°C for eight hours, the maghemite and magnetite diffraction peaks disappeared and phase pure polycrystalline hematite was obtained as seen in figure 2.a. An XRD spectra for annealed iron oxide deposited on FTO is given in figure 2.b, showing the presence of hematite as well as cassiterite, SnO_2 from the substrate, but no other phases. The hematite peaks in figure 2.b are relatively weak compared with the SnO_2. This is because the θ-2θ geometry make the underlying layer more visible compared to the GIXRD. All the XRD measurements showed the same result after heat treatment at 500°C regardless of the substrate.

From XRF measurements the Fe-mass was extracted, which together with XRR-measurements on films deposited on Si were used to give a first measure of the film thicknesses. This is described in more depth in the supporting information.

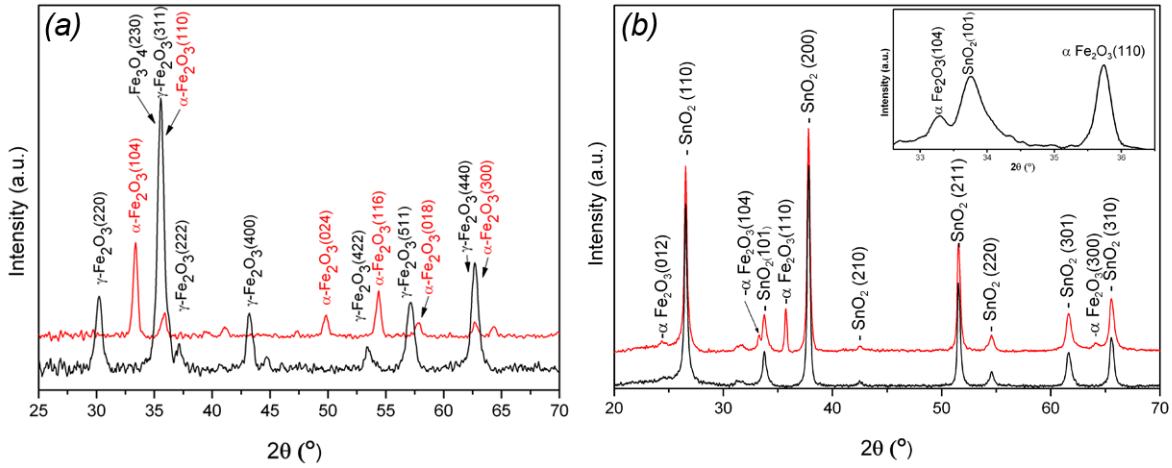

Figure 2. (a) Iron oxide deposited on Si(100). The black line is for an as deposited film and the red line is for the same film after heat treatment at 500°C. (b) Diffraction pattern for a film deposited on FTO after annealing at 500°C (red line) and for a FTO reference sample (black line). In the upper right corner is a zoom over the two strongest hematite peaks.

Raman spectroscopy measurements on the as deposited films revealed three clearly visible peaks at 298 cm^{-1}, 523 cm^{-1} and 666 cm^{-1}, that can be ascribed to magnetite.
After annealing these peaks disappears, and only hematite peaks occur in the post annealed films as seen in figure 3. This is in agreement with the XRD results showing a phase transformation into hematite upon heat treatment. In figure 3.b it is clearly seen that no peaks shift in energy with regard to thickness, indicating negligible strain.

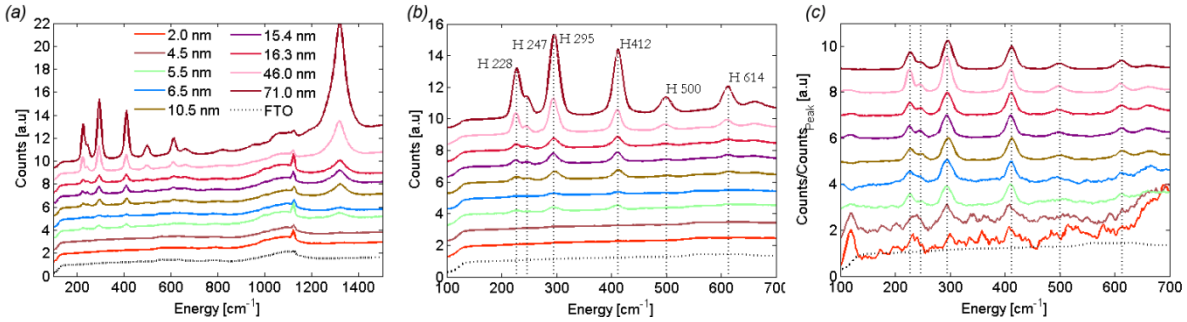

Figure 3. (a) Raman data for a subset of the annealed films. Data is shifted in height to ease the interpretation. (b) The same data but in a smaller energy range with the hematite peaks labeled. (c) The background have been removed and the data have been normalized with respect to the peak height for the vibration at 412 cm^{-1}

Hematite have a corundum crystal structure and can be classified in the D^6_{3d} space group[62] with five E_g phonon modes and two A_{1g} modes expected in the Raman spectrum below 700 cm^{-1}. Raman measurements on bulk hematite in literature show five E_g modes at 246, 293, 299, 411, and 612 cm^{-1} and two A_{1g} modes at 227 and 612 cm^{-1}[63] when using low laser light intensity (0.7mW) and a peak dependent shift of up to 14 cm^{-1} when using higher laser intensity (7mW). The broadening at room temperature makes the two closest E_g modes (293 and 299 cm^{-1}) in practice indistinguishable and one would expect to resolve four E_g modes at ambient conditions. For the low-dimensional hematite we find bands that can be assigned the four E_g modes at 247, 295, 412, and 614 cm^{-1} and two A_{g1} modes at 228 and 500 cm^{-1} in very good agreement (within 2 cm^{-1}) with careful Raman measurements performed with low laser intensity.

In order to compare the relative intensities of the different peaks with regard to film thickness, the background was removed and the data normalized with respect to the peak height for the vibration at 412 cm^{-1} as shown in figure 3.c. All the peaks labeled in figure 3.b then appear to be of almost the same relative height except a slight suppression of the 297cm^{-1} peak assigned as an E_g mode. The noise level for the 4.5 nm film is considerably higher than for the thicker films, and for films with even thinner nominal thickness the Raman detection limit was too low. The data show no anisotropic phonon confinement in films thicker than 5 nm as no relative peak intensities, shifts or selective broadening could be detected when low laser intensity was used. The Raman data show a general suppression of all phonon modes with a slightly stronger suppression of the 297cm^{-1} E_g mode. The general suppression thus seems to be an effect of isotropic phonon confinement. Note that thinner films also will give less Raman intensity due to less material.

To investigate the morphology of the deposited and annealed films SEM images were taken of films of different thicknesses as seen in figure 4. Additional SEM images are found in the supporting information. The middle figure shows that the film start to grow as islands which then coalesce to a film. This is in very good agreement with the behavior of ultrathin films of iron oxide on more perfect substrates such as Pt(100)[64], Si(100) and SiO_2[18].

The coalescence seems to occur around a nominal film thickness of 10 nm which is similar to the thickness where the Raman intensity increases more markedly. That is an indication that the films demand a certain thickness or a certain amount of material until a more completely crystallization into hematite occur. The thicker films are not atomically smooth, but have a distinct microstructure as seen in figure 4.c. This is probably a consequence of decomposition of the iron precursor in the gaseous phase, which results in a somewhat more CVD like growth behavior.

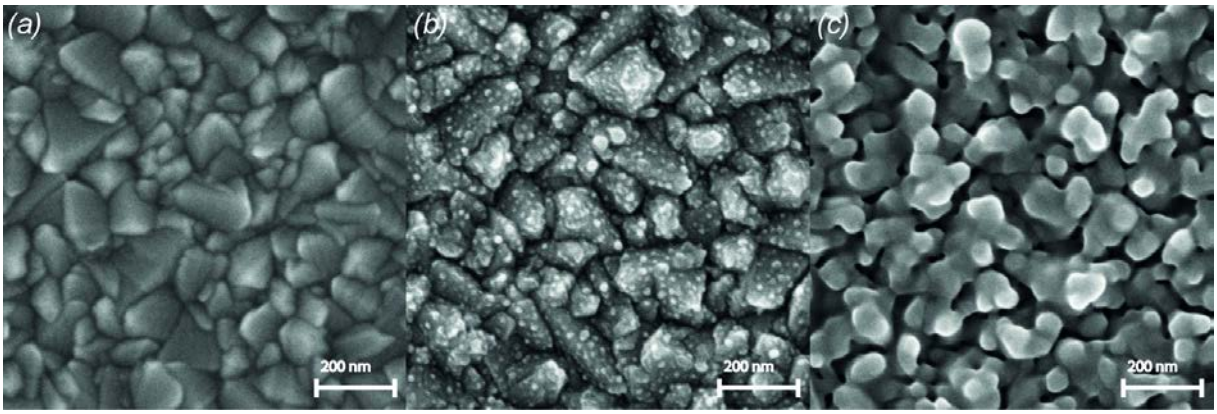

Figure 4. (a) FTO reference sample (b) ~ 4 nm iron oxide on top of FTO (c) ~30 nm iron oxide on top of FTO. The magnification is the same in all figures.

X-ray photoelectron spectroscopy, XPS, was used to determine the chemical composition of the films and to investigate possible impurities. XPS spectra of the films showed carbon on the surface, but just under the surface and within the films the carbon signal decreased down to the detection limit of the instrument which is below 1 %. The origin of the carbon on the outer most surface can be attributed to exposure of the samples to air prior to the analysis. The total absent of carbon within the film shows that all the ligands of the $Fe(CO)_5$ reacted with oxygen or decomposed from the surface at 300°C, and where removed by the purge pulses as intended, and not incorporated into the films. The XPS-data are found in the supporting information.

Near the surface, the atomic ratio of iron to oxygen was close to the expected value of 2 to 3 corresponding to Fe_2O_3. No reliable data concerning the iron to oxygen ratio can however be obtain deeper down in the film due to preferential sputtering of oxygen which is a well known problem for depth profiling with XPS[65-67].

4.3. Optical quantum confinement

Transient absorption measurements were performed on the films deposited on FTO, and raw data is presented in figure 5.a. The film thicknesses were determined by combining the XRR and XRF measurements as described in section 3.2. In figure 5.b these values are related to the maximum absorption in figure 5.a. Both these are a measure on film thickness as verified by the direct correlation seen in the figure. Ideally a straight line is expected. A linear relation is also obtained, with some minor scattering in the data due to the surface roughness of the FTO.

The consistency between the value of the absorption maximum and the thickness estimate from XRF allows an estimation of the absorption coefficient for the absorption maximum close to 400nm to be made. This gives a value of α_{max} of $1.6 \cdot 10^5$ cm^{-1} with a standard deviation of $0.30 \cdot 10^5$ cm^{-1} (figures of this can be found in the supporting information). Within the resolution of the measurement no thickness dependence of this value is found, but the data scatter to some extent so a small effect cannot be excluded. In the calculations no such effect is assumed and the mean value of α_{max} has been used. This value correlate well with values previously reported in the literature[15, 68].

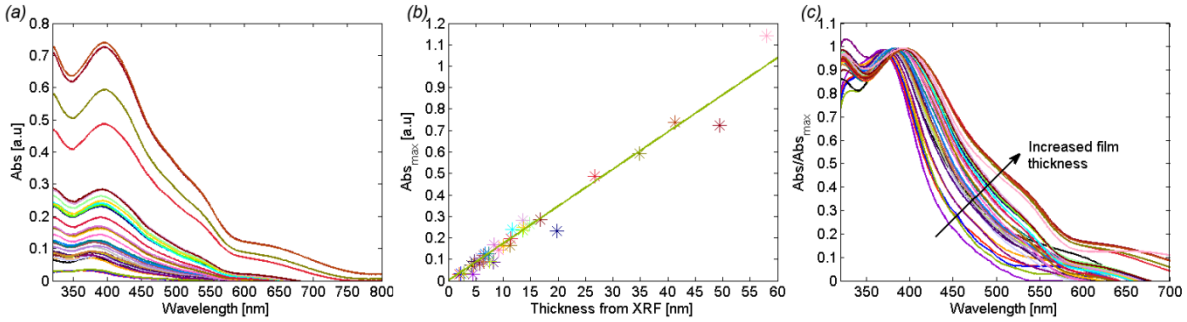

Figure 5 (a). Absorption as a function of wavelength for all samples. Figures with different scaling are found in the supporting information to resolve data for the thinnest films. (b) Absorption maximum compared to estimated film thickness from XRF measurements. (c) Absorption data normalized with respect to the absorption peak value.

According to Lambert-Beers law absorption is linear with respect to optical path length, which is equivalent to film thickness in this case. Given the absorption coefficient, preferably at the absorption maximum, the film thicknesses could be determined form the absorption data.

Given the estimated value of α_{max} the film thicknesses are reevaluated by using the absorption data in figure 5.a. By using the statistics from all the XRF measurements this gives a more accurate determination, which is used in the subsequent analysis. The relation between the first thickness estimates from XRF and the values from the processed absorption data is in very good agreement. Data for this are found in the supporting information. The thickness given here is an effective volume averaged thickness evening out microscopic irregularities due to island formation for the thinnest films. The absorption coefficients for different selected wavelengths are given in table 2. Notice that this represents a mean absorption coefficient, and as described below there is a thickness dependence in the visible for the thinner films.

Table 2. Absorption coefficient, $\alpha(\lambda)$, at different wavelengths for α-Fe_2O_3, (hematite). A full list with all the wavelengths measured is found in the supporting material.

Wavelength [nm]	Energy [eV]	α [10^5 cm^{-1}]
350	3.55	1.416
400	3.10	1.578
450	2.76	1.104
500	2.48	0.718
550	2.26	0.432
600	2.07	0.204

Given the film thickness correlating well with the absorption data in figure 5.a the absorption coefficient as a function of both wavelength and film thickness are easily calculated and both figures as well as the entire dataset are found in the supporting information. The incoming light was held perpendicular to the films and a collimating lens was used behind the films for an effective collection of scattered light to the CCD detector to minimize the error from scattering losses. The reported values will represent a higher limit due to neglect of reflection losses. The Absorption, *A*, and the absorption coefficient are here given based on the tenth logarithm as in eqn. (13) where *I* is transmitted intensity, I_o incident intensity, α absorption coefficient, and *d* optical path length of the material. This is the common convention in the field of chemistry contrasting the field of physics where absorption commonly is reported based on the natural logarithm. The values can easily be converted by multiplication of *ln(10)*.

$$A = -\log_{10}\left(\frac{I}{I_0}\right) = \alpha d \qquad (13)$$

To more easily compare the absorption behavior for the different films data are normalized with respect to the absorption maximum as in figure 5.c. Two interesting effects are then immediately evident. The absorption maximum, even though constant in intensity as seen above, is shifted to lower wavelengths for thicker films as illustrated in figure 6.a-b. This shift is in the order of 200 meV while going from film thicknesses of 4 to 20 nm, where after it levels of towards the bulk value. A blue shift of the absorption edge is a clear sign of quantum confinement and is commonly found in other materials[41] whereas here we also see a change of the position of the absorption maximum. Since the absorption probability is a function of the interaction Hamiltonian and the joint density of states between the initial and final states as in eqn. (9) this indicates either a change in the orbital overlap or in the density of states in the initial and final states for ultrathin hematite. A clear thickness dependence is also evident for the absorption between 450 and 650 nm where it gets distinctly weaker with decreased film thickness, as seen in figure 5.c and visualized in the contour plot in figure 6.c.

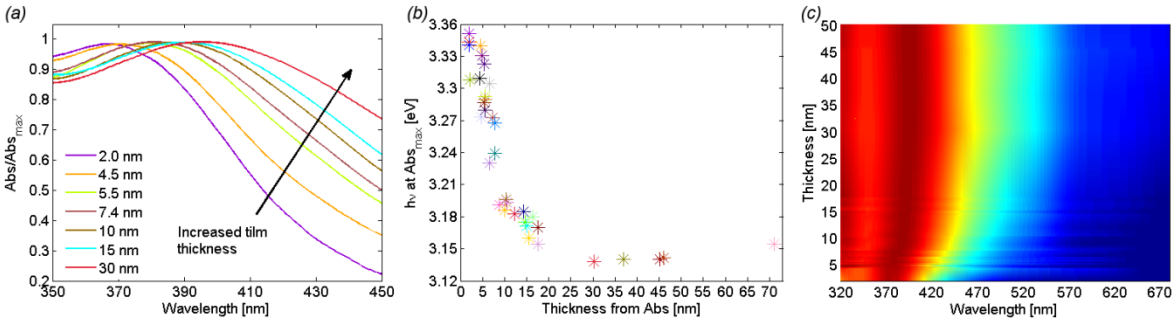

Figure 6. (a) Shift of absorption maximum as a function of film thickness. (b) The photon energy corresponding to the absorption peak as a function of film thickness. (c) A couture plot of the data in 5.c where normalized absorption are given as a function of film thickness and wavelength.

A qualitative understanding for the absorption behavior in the bulk can in principle be obtain by analyzing the electronic band structure, given in the theory section[35] in figure 1.a. The calculated data qualitatively show both an indirect and a direct transition which readily should be possible to resolve in the experimental UV-vis data.

The experimental values for the indirect band gap, as reported in the literature, scatter between approximately 1.9-2.2 eV[9, 69]and depends to some degree on the route of synthesis. All indirect semiconductors also have direct transitions at higher energies. Quantum confinement due to decreased film thickness could potentially affect both the position of the indirect and direct band gaps as well as the probability for these transitions to occur.

As discussed in the theory section the indirect band gap scales as the square of the energy difference between the band gap and the phonon energy, $\hbar\omega$, as in eqn. (14). The indirect band gap could thus be extracted by plotting the square root of the absorption against photon energy and extrapolate to zero absorption, as shown for a subset of the films in figure 7.a. The entire dataset is found in the supporting information.

$$A \propto \left(\hbar\omega - E_g\right)^2 \qquad (14)$$

A linear region is there found in an energy interval of approximately 2.17-2.27 eV. This behavior is however less distinct for the thinner films and completely absent for the thinnest films. The transition region where the model fails and the data starts to scatter considerably is between 5 and 6 nm, and for films under 4 nm it is not valid at all. Until this point is reached a blue shift in the indirect band gap in the order of 0.3 eV is observed while going to thinner films as illustrated in figure 7.b. The slope of the linear region is a measure of the absorption coefficient in this region and thus also of the transition probability. Comparing normalized absorption gives that this transition probability is fairly constant down to film thicknesses around 10 nm where after it rapidly decreases as seen in figure 7.c. This is in line with the diminishing and final disappearance of the indirect transition and the failure of the model for the thinnest films. This could either be due to a decreased joint density of states or a reduced photon-phonon coupling, or even a decreased orbital overlap.

The values here obtained for the indirect band gap starts at 1.75 eV for the thickest films and increases too slightly above 2 eV while the transition disappears. This is in the lower range of the values reported in the literature. The analysis to obtain the indirect band gap relies on taking the square root of the measured data. This has the mathematical consequence of increasing the noise in the signal. The effects of light scattering, the Urbach tail and absorption due to imperfections thus increases in importance. Both the magnitude of the signal as well as the intercept of the interpolation can shift as a consequence of this, which

accounts both for the scatter in the data reported here as well as the different values reported in the literature. Trends in samples made under similar conditions, however, should be accurate and advisable to use.

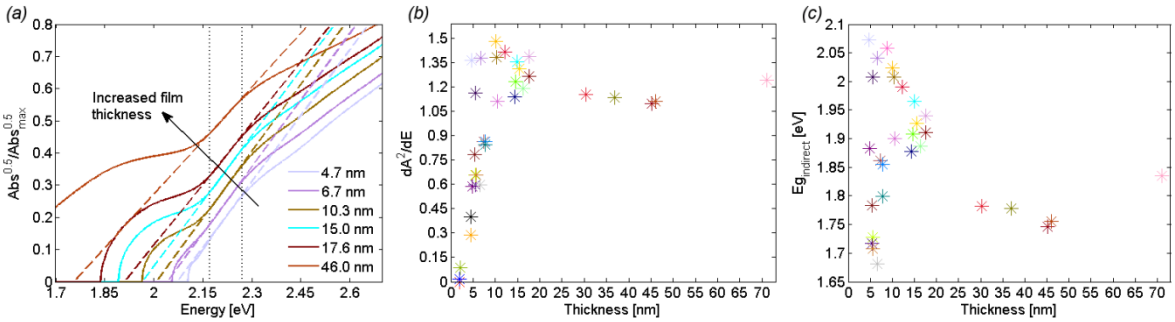

Figure 7 (a) Square root of normalized absorption data against photon energy for a subset of the samples. (b) Energetic position of the indirect band gap as a function of film thickness. (c) Slope of the linear region in (a) as a function of film thickness.

Rationalization of this behavior can be given by correlating the absorption to the phonon behavior, as an indirect transition involves both the absorption of a photon as well as the momentum transfer by a phonon. A reasonable hypothesis is that the small dimensions in the thinnest films will lead to a spatial confinement and a suppression of the phonons, which is known to occur for other materials[42]. This would decrease the probability for the photon-phonon interaction necessary for the indirect transition pictured in figure 1 and would be in line with the experimental data in figure 7. The Raman data in figure 3 give an indication that the phonons are collectively suppressed for the thinner films and absent for the ones below 4 nm. The origin of this effect can however also be due to lack of Raman cross-section for the thinnest films, which also would be manifested as less intense phonons. Since the absorption in the UV-vis still shows a high cross-section for the thinnest films, lack of Raman cross-section cannot be the sole explanation to the depression of the Raman signal. Effects from island formations for the thinnest films would suppress phonons modes more selective and is also not seen. The decrease in the amplitude of the indirect transition with thinner films is an interesting finding and of importance while designing geometries for absorption purposes.

All indirect semiconductors do by necessity also have direct transitions at higher photon energies not involving phonon interactions. For such a transition, as described in the theory section, the absorption will in a limited energy interval, provided that the bands can be described as parabolas with respect to crystal momentum, be proportional to the square root of the energy difference between the energy of the light and the band gap according to eqn. (15).

$$A \propto \left(\hbar\omega - E_g\right)^{1/2} \qquad (15)$$

The direct band gap can thus be extracted by plotting the square of the absorption and extrapolate the straight region for photon energies slightly above the band gap energy down to zero absorption. For an indirect semiconductor this process is overlaid on absorption due to the indirect transition which to some extent interferes with the analysis. The direct transition is a considerably more probable process, thus overshadowing the indirect transition and thereby renders the analysis fairly accurate in practice.

The square of the absorption is plotted against photon energy for a subset of the samples in figure 8.a, and it appears to be two regions with linear character, one between 2.45-2.60 eV and one at slightly higher energies. The first region indicate a direct transition around 2.15 eV for thicker films which according to the calculated band diagram in figure 1.a likely correspond to the principal direct transition at the Γ-point. Also for this transition a blue shift

is seen for the thinner films as seen in figure 8.b, and for the thinnest films the shift is as large as 0.3 eV compare to the bulk. For the other direct transition, which seems to give a stronger absorption, the blue shift is even larger and in the order of 0.45 eV. The categorization of this transition is more difficult as the theoretical band diagrams give several possible alternatives, and it is also overlaid on the lower energy transitions. This is in some sense reflected in the stronger absorption.

The blue shift starts for film thicknesses around approximately 20 nm and accelerates for thinner films, which is in line with the behavior for the indirect transition. The data for the direct transition scatters less than for the indirect transition, which is an effect of squaring the absorption data and thus decreasing the impact of non ideal absorption processes.

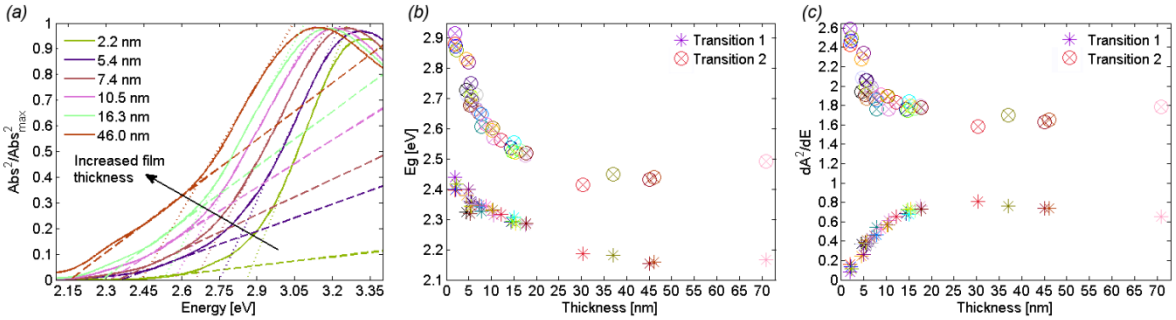

Figure 8 (a) Square of normalized absorption data against photon energy for a subset of the samples. (b) Energetic position of the two direct transitions as a function of film thickness. (c) Slope of the linear regions in (a) as a function of film thickness.

The slope of the linear regions in figure 8.a corresponds to the probability of the respective transitions. These changes rather dramatically with film thickness as illustrated in figure 8.c. The first direct transition start to decrease around 20 nm and reaches very low transition probabilities for the thinnest films, whereas for the second direct transition the slope of the linear region increases with approximately the same amount. It thus appears that for thinner films the absorption probability for more energetic photons is increased at the expense of the absorption of less energetic photons. This behavior can be rationalized with an electronic quantum confinement in the thin films, decreasing the density of states for the lowest lying conduction band states at the Γ-point. Another possibility that may explain part of the observed phenomena is strain caused by lattice miss match between the α-Fe_2O_3 and the underlying substrate. Strain is however not likely to be the dominant mechanism as no measurable peak shifts could be seen in the Raman spectra. Post annealing is known to decrease stress and for the very thinnest films, where the effect is largest, the stress should supposedly be somewhat less due to island formation. If strain were present, there would likely be gradients in the stress across the films, making it reasonable to assume less sharp and more smeared out absorption characteristics than what here is observed.

A graphical summary of the findings is given in figure 9. To summarize, there is a clear blue shift of the absorption maximum between 4-20 nm nominal film thickness showing a change in the electronic structure indicating either change in orbital overlap or density of states for low-dimensional hematite. There is a blue shift of the absorption edge for all transitions, direct and indirect, for films thinner than approximately 20 nm. It is also observed that the absorption probability for the indirect transition at longer wavelengths get less probable for the thinner films. This is important and highly disadvantageous for the use of thin films of hematite in for example solar water splitting applications, in the sense that the optical path length of ultrathin hematite films in a nanostructure arrays needs to be thicker than what would be expecting based on the optical properties of bulk hematite. Given the

transport limitations of hematite the layers needs to be thin enough for these effects to be of importance, meaning that the full absorption potential of bulk hematite probably not can be utilized unless the transport properties are improved, by for example doping. These data are obtain for reasonable flat films, but the conclusions should be directly transferable to more complicated three dimensional geometries, and will be of importance in the design of hematite nanostructures for absorption and transport properties.

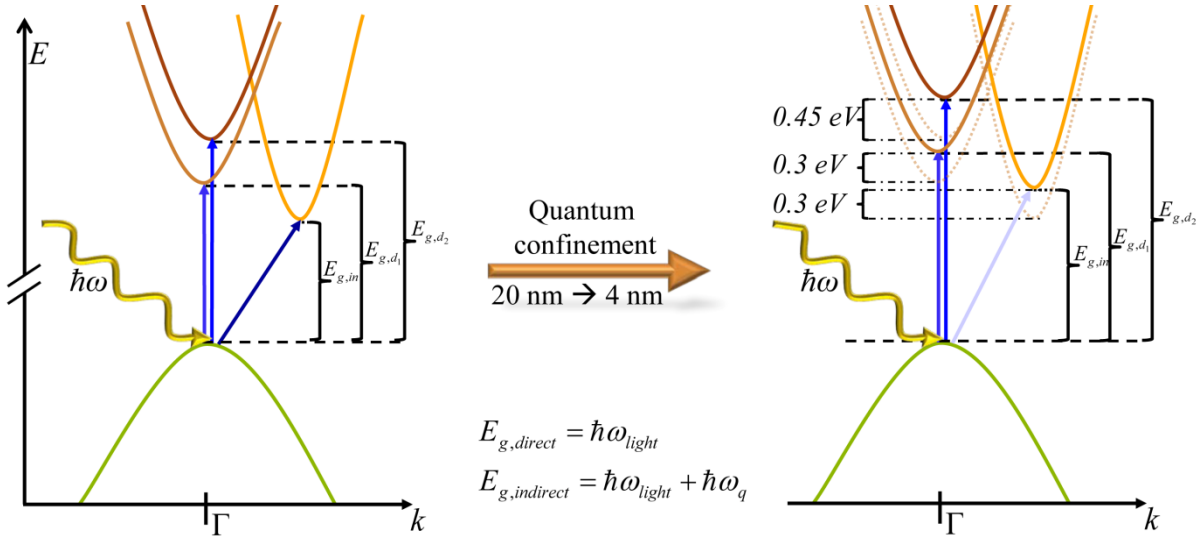

Figure 9. A schematic summary of the different optical quantum confinement effects found for low dimensional hematite

5. Summary and Conclusions

A series of ultrathin films of hematite have been synthesized from gas phase precursors, giving films of high quality, from which the absorption properties have been investigated. We find that the absorption maximum shifts towards higher energies for films thinner than 20 nm, revealing that the electronic structure is changed for hematite with dimensions smaller than that. This is indicative of either decreased orbital overlap or change in the density of states in the valence and the conduction band, which is investigated in some detail here. For thinner films a substantial blue shift of the absorption edge is also observed for all transitions, both for the indirect and the direct ones. The indirect transition gets weaker and less probable for thinner films and essentially disappears for films thinner than 5-6 nm. A possible explanation for this is phonon suppression due to spatial confinement in the thinnest films. The transition probability for the first direct transition also decreases with thinner film thickness, whereas it increases somewhat for higher photon energies. This could be rationalized by an electronic quantum confinement shifting part of the conduction band energy levels and thereby increasing the DOS higher up in conduction band.

These findings are of great importance as they in some detail analyze both the indirect and direct transitions in the optical transitions in hematite as well as points at a so far rather undiscussed problem with the use of hematite as an absorber material for solar water splitting and other light active applications. The limited charge carrier transport distance compared to the absorption coefficient is often emphasized as the Achilles heel of hematite. The suggested solution to this problem is to ortogonalize the absorption from the transport by nanostructuration, but this work indicate that this approached may give worse results than first anticipated. If the absorbing layers get sufficiently thin with respect to the hole transport properties, the absorption for the longer, more abundant wavelengths in the visible, become a less probable process and eventually disappear for thin enough films. It will thus be hard to realize the full absorption potential of bulk hematite unless the transport properties could be improved. Nanoscale hematite could still be of great interest and with this increased knowledge concerning the absorption processes for the indirect and direct transitions it will be easier to aim for the best possible low-dimensional structures that could realize as much as possible of the potential of hematite.

6. Supporting information

Calibration curve for film thicknesses estimated from XRR and XRF measurements. Additional SEM figures. XPS data. A version of figure 5.a split into four individual figures. A second version of figure 5.b. Maximum absorption coefficient as a function of wavelength. A comparison between the thickness estimates based on XRR/XRF and the processed absorption data. Mean absorption coefficient as a function of wavelength. The complete dataset or the absorption as a function of both wavelength and film thickness. The complete dataset for the determination of the indirect band gap extending figure 7.a in the main article. The complete dataset for the determination of the direct transitions extending figure 8.a in the main article. A table summarizing all the key data. These data are available free of charge via the internet at …

7. Acknowledgements

We are grateful for financial support from Ångpanneföreningens forskningsstiftelse and the Swedish Energy Agency.

8. References

1. J. Liu, Y. Li, H. Fan, Z. Zhu, J. Jiang, R. Ding, Y. Hu and X. Huang, *Chemistry of Materials*, 2010, **22**, 212-217.
2. C. Wu, P. Yin, X. Zhu, C. OuYang and Y. Xie, *Journal of Physical Chemistry B*, 2006, **110**, 17806-17812.
3. L.-S. Zhong, J.-S. Hu, H.-P. Liang, A.-M. Cao, W.-G. Song and L.-J. Wan, *Advanced Materials*, 2006, **18**, 2426-2431.
4. M. S. Islam, Y. Kusumoto, M. Abdulla-Al-Mamun and Y. Horie, *Chemistry Letters*, 2011, **40**, 773-775.
5. X. Gou, G. Wang, X. Kong, D. Wexler, J. Horvat, J. Yang and J. Park, *Chemistry-a European Journal*, 2008, **14**, 5996-6002.
6. J. H. Kennedy and K. W. Frese, *J. Electrochem. Soc.*, 1978, **125**, 709-714.
7. K. Sivula, F. Le Formal and M. Graetzel, *Chemsuschem*, 2011, **4**, 432-449.
8. M. J. Katz, S. C. Riha, N. C. Jeong, A. B. F. Martinson, O. K. Farha and J. T. Hupp, *Coord. Chem. Rev.*, 2012, **256**, 2521-2529.
9. D. A. Wheeler, G. M. Wang, Y. C. Ling, Y. Li and J. Z. Zhang, *Energy & Environmental Science*, 2012, **5**, 6682-6702.
10. D. K. Bora, A. Braun and E. C. Constable, *Energy & Environmental Science*, 2013, **6**, 407-425.
11. K. Sivula, F. Le Formal and M. Gratzel, *Chemsuschem*, 2011, **4**, 432-449.
12. N. Beermann, L. Vayssieres, S. E. Lindquist and A. Hagfeldt, *J. Electrochem. Soc.*, 2000, **147**, 2456-2461.
13. S. K. Mohapatra, S. E. John, S. Banerjee and M. Misra, *Chem. Mater.*, 2009, **21**, 3048-3055.
14. A. Kay, I. Cesar and M. Gratzel, *J. Am. Chem. Soc.*, 2006, **128**, 15714-15721.
15. K. Sivula, R. Zboril, F. Le Formal, R. Robert, A. Weidenkaff, J. Tucek, J. Frydrych and M. Gratzel, *J. Am. Chem. Soc.*, 2010, **132**, 7436-7444.
16. L. Vayssieres, C. Sathe, S. M. Butorin, D. K. Shuh, J. Nordgren and J. H. Guo, *Adv. Mater.*, 2005, **17**, 2320-2323.
17. J. Wang, W. B. White and J. H. Adair, *J. Am. Ceram. Soc.*, 2005, **88**, 3449-3454.
18. I. Jõgi, J. T. Jacobsson, M. Fondell, J. T. Wätjen, J. O. Carlsson, M. Boman and T. Edvinsson, *Submitted to Thin Solid Films*, 2013.
19. P. Hiralal, S. Saremi-Yarahmadi, B. C. Bayer, H. L. Wang, S. Hofmann, K. G. U. Wijayantha and G. A. J. Amaratunga, *Sol. Energy Mater. Sol. Cells*, 2011, **95**, 1819-1825.
20. H. Jiao and G. S. Jiao, *Mater. Lett.*, 2009, **63**, 2725-2727.
21. K. Woo, H. J. Lee, J. P. Ahn and Y. S. Park, *Adv. Mater.*, 2003, **15**, 1761-1764.
22. Y. S. Hu, A. Kleiman-Shwarsctein, A. J. Forman, D. Hazen, J. N. Park and E. W. McFarland, *Chem. Mater.*, 2008, **20**, 3803-3805.
23. A. Duret and M. Gratzel, *J. Phys. Chem. B*, 2005, **109**, 17184-17191.
24. B. M. Klahr, A. B. F. Martinson and T. W. Hamann, *Langmuir*, 2011, **27**, 461-468.
25. I. Cesar, K. Sivula, A. Kay, R. Zboril and M. Graetzel, *J. Phys. Chem. C*, 2009, **113**, 772-782.

26. W. Heitler, *The Quantum Theory of Radiation*, Oxford University Press, Oxford, 1960.
27. R. Loudon, *The Quantum Theory of Light*, Oxford University Press, UK, 2010.
28. P. A. M. Dirac, *Proc. R. Soc. A*, 1927, **114**, 243-265.
29. M. Lax, *J. Chem. Phys.*, 1952, **20**, 1752-1760.
30. L. H. Hall, J. Bardeen and F. J. Blatt, *Proc. of Atlantic City Photoconductivity Conference 1954*, New York, 1956.
31. L. H. Hall, J. Bardeen and F. J. Blatt, *Phys. Rev*, 1954, **95**, 559-560.
32. B. K. Ridley, *Quantum Processes in Semiconductors*, Oxford University Press, Cryodon, UK, 2013.
33. R. J. Elliott, *Phys. Rev*, 1957, **108**, 1384-1389.
34. T. S. Mott, *Optical Properties of Semi-Conductors*, Butterworths Scientific Publications, Belfast, Northern Ireland, 1959.
35. Anubhav Jain, Shyue Ping Ong, Geoffroy Hautier, Wei Chen, William Davidson Richards, Stephen Dacek, Shreyas Cholia, Dan Gunter, David Skinner, Gerbrand Ceder and K. A. Persson, *APL Materials*, 2013, **1,** 011002-011002-11.
36. A. Bertoni, M. Royo, F. Mahawish and G. Goldoni, *Phys. Rev. B*, 2011, **84**, 205323-205323-9.
37. B. M. Wong, F. Leonard, Q. M. Li and G. T. Wang, *Nano Lett.*, 2011, **11**, 3074-3079.
38. R. C. Iotti and L. C. Andreani, *Phys. Rev. B*, 1997, **56**, 3922-3932.
39. T. J. Jacobsson and T. Edvinsson, *J. Phys. Chem. C*, 2013, **117**, 5497-5504.
40. T. J. Jacobsson and T. Edvinsson, *J. Phys. Chem. C*, 2012, **116**, 15692-15701.
41. T. J. Jacobsson and T. Edvinsson, *Inorg. Chem.*, 2011, **50**, 9578-9586.
42. D. Raymand, T. J. Jacobsson, K. Hermansson and T. Edvinsson, *J. Phys. Chem. C*, 2012, **116**, 6893-6901.
43. R. L. Puurunen, *J. Appl. Phys.*, 2005, **97,** 121301-121301-52.
44. A. G. Gilbert and K. G. Sulzmann, *J. Electrochem. Soc.*, 1974, **121**, 832-834.
45. M. Aronniemi, J. Saino and J. Lahtinen, *Thin Solid Films*, 2008, **516**, 6110-6115.
46. O. Nilsen, M. Lie, S. Foss, H. Fjellvag and A. Kjekshus, *Appl. Surf. Sci.*, 2004, **227**, 40-47.
47. P. Zhang, A. Kleiman-Shwarsctein, Y. S. Hu, J. Lefton, S. Sharma, A. J. Forman and E. McFarland, *Energy & Environmental Science*, 2011, **4**, 1020-1028.
48. M. de Ridder, P. C. van de Ven, R. G. van Welzenis, H. H. Brongersma, S. Helfensteyn, C. Creemers, P. Van Der Voort, M. Baltes, M. Mathieu and E. F. Vansant, *J. Phys. Chem. B*, 2002, **106**, 13146-13153.
49. K. Zhou, J. Q. Huang, Q. Zhang and F. Wei, *Nanoscale Research Letters*, 2010, **5**, 1555-1560.
50. L. Hannevold, O. Nilsen, A. Kjekshus and H. Fjellvag, *Appl. Catal., A*, 2005, **284**, 177-184.
51. J. A. Libera, J. W. Elam, N. F. Sather, T. Rajh and N. M. Dimitrijevic, *Chem. Mater.*, 2010, **22**, 409-413.
52. M. Lie, H. Fjellvag and A. Kjekshus, *Thin Solid Films*, 2005, **488**, 74-81.

53. M. Rooth, A. Johansson, K. Kukli, J. Aarik, M. Boman and A. Harsta, *Chem. Vap. Deposition*, 2008, **14**, 67-70.
54. J. R. Scheffe, A. Frances, D. M. King, X. H. Liang, B. A. Branch, A. S. Cavanagh, S. M. George and A. W. Weimer, *Thin Solid Films*, 2009, **517**, 1874-1879.
55. I. L. Soroka, M. Rooth, J. Lu, M. Boman, P. Svedlindh, J. O. Carlsson and A. Harsta, *J. Appl. Phys.*, 2009, **106,** 084313-084313-7.
56. J. Escrig, J. Bachmann, J. Jing, M. Daub, D. Altbir and K. Nielsch, *Phys. Rev. B*, 2008, **77,** 214421-214421-7.
57. X. Li, N. C. Fan and H. J. Fan, *Chem. Vap. Deposition*, 2013, **19**, 104-110.
58. K. Pitzschel, J. M. M. Moreno, J. Escrig, O. Albrecht, K. Nielsch and J. Bachmann, *ACS Nano*, 2009, **3**, 3463-3468.
59. B. S. Lim, A. Rahtu and R. G. Gordon, *Nat. Mater*, 2003, **2**, 749-754.
60. J. Bachmann, J. Escrig, K. Pitzschel, J. M. M. Moreno, J. Jing, D. Gorlitz, D. Altbir and K. Nielsch, *J. Appl. Phys.*, 2009, **105,** 07B521.
61. J. Bachmann, J. Jing, M. Knez, S. Barth, H. Shen, S. Mathur, U. Gosele and K. Nielsch, *J. Am. Chem. Soc.*, 2007, **129**, 9554-9555.
62. S. P. S. Porto and R. S. Krishnan, *J. Chem. Phys.*, 1967, **47**, 1009-1012.
63. D. L. A. deFaria, S. V. Silva and M. T. deOliveira, *J. Raman. Spectrosc*, 1997, **28**, 873-878.
64. W. Weiss and W. Ranke, *Prog. Surf. Sci.*, 2002, **70**, 1-151.
65. A. M. Andersson, A. Henningson, H. Siegbahn, U. Jansson and K. Edstrom, *J. Power Sources*, 2003, **119**, 522-527.
66. K. Edstrom, M. Herstedt and D. P. Abraham, *J. Power Sources*, 2006, **153**, 380-384.
67. E. Lewin, M. Gorgoi, F. Schafers, S. Svensson and U. Jansson, *Surface & Coatings Technology*, 2009, **204**, 455-462.
68. F. L. Souza, K. P. Lopes, P. A. P. Nascente and E. R. Leite, *Sol. Energy Mater. Sol. Cells*, 2009, **93**, 362-368.
69. L. Vayssieres, in *Solar Hydrogen and Nanotechnology*, ed. L. Vayssieres, 2006, pp. U191-U200.

Optical Quantum Confinement in Low Dimensional Hematite

Table of contents entry: Color graphics

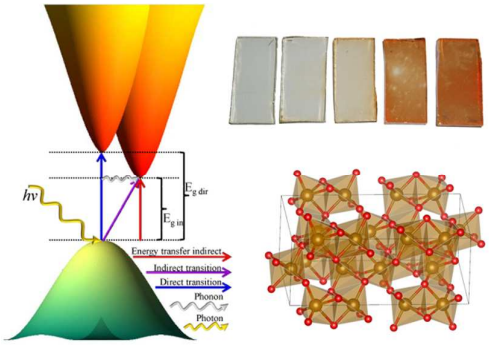

Optical and vibrational properties in low dimensional hematite are investigated where the indirect transition essentially disappears for the thinnest films.